Review of Scientific Instruments

Single frequency thermal wave radar: A next-generation dynamic thermography for quantitative non-destructive imaging over wide modulation frequency ranges

Cite as: Rev. Sci. Instrum. **89**, 044901 (2018); https://doi.org/10.1063/1.5016339
Submitted: 17 November 2017 . Accepted: 12 March 2018 . Published Online: 04 April 2018

Alexander Melnikov, Liangjie Chen, Diego Ramirez Venegas, Koneswaran Sivagurunathan, Qiming Sun, Andreas Mandelis, and Ignacio Rojas Rodriguez

View Online Export Citation CrossMark

ARTICLES YOU MAY BE INTERESTED IN

Thermal-wave radar: A novel subsurface imaging modality with extended depth-resolution dynamic range
Review of Scientific Instruments **80**, 034902 (2009); https://doi.org/10.1063/1.3095560

Perspective: Principles and specifications of photothermal imaging methodologies and their applications to non-invasive biomedical and non-destructive materials imaging
Journal of Applied Physics **124**, 160903 (2018); https://doi.org/10.1063/1.5044748

Three-dimensional thermographic imaging using a virtual wave concept
Journal of Applied Physics **121**, 105102 (2017); https://doi.org/10.1063/1.4978010

MCL
MAD CITY LABS INC.
www.madcitylabs.com

Nanopositioning Systems

Modular Motion Control

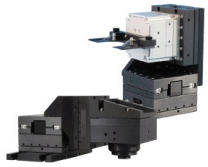

AFM and NSOM Instruments

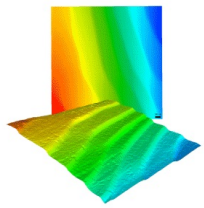

Single Molecule Microscopes

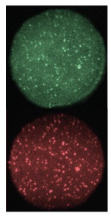

AIP Publishing

© 2018 Author(s).

REVIEW OF SCIENTIFIC INSTRUMENTS **89**, 044901 (2018)

Single frequency thermal wave radar: A next-generation dynamic thermography for quantitative non-destructive imaging over wide modulation frequency ranges

Alexander Melnikov,[1] Liangjie Chen,[1] Diego Ramirez Venegas,[1,2] Koneswaran Sivagurunathan,[1] Qiming Sun,[1,3] Andreas Mandelis,[1,3,a)] and Ignacio Rojas Rodriguez[2]

[1]*Center for Advanced Diffusion-Wave and Photoacoustic Technologies (CADIPT), University of Toronto, Toronto M5S 3G8, Ontario, Canada*

[2]*Technological University of Queretaro (UTEQ), Pie de la Cuesta Avenue 2501, Unidad Nacional, Queretaro, Mexico*

[3]*School of Optoelectronic Information, University of Electronic Science and Technology of China, Chengdu 610054, China*

(Received 17 November 2017; accepted 12 March 2018; published online 4 April 2018)

Single-Frequency Thermal Wave Radar Imaging (SF-TWRI) was introduced and used to obtain quantitative thickness images of coatings on an aluminum block and on polyetherketone, and to image blind subsurface holes in a steel block. In SF-TWR, the starting and ending frequencies of a linear frequency modulation sweep are chosen to coincide. Using the highest available camera frame rate, SF-TWRI leads to a higher number of sampled points along the modulation waveform than conventional lock-in thermography imaging because it is not limited by conventional undersampling at high frequencies due to camera frame-rate limitations. This property leads to large reduction in measurement time, better quality of images, and higher signal-noise-ratio across wide frequency ranges. For quantitative thin-coating imaging applications, a two-layer photothermal model with lumped parameters was used to reconstruct the layer thickness from multi-frequency SF-TWR images. SF-TWRI represents a next-generation thermography method with superior features for imaging important classes of thin layers, materials, and components that require high-frequency thermal-wave probing well above today's available infrared camera technology frame rates. *Published by AIP Publishing.*
https://doi.org/10.1063/1.5016339

I. INTRODUCTION

Lock-in thermography imaging (LITI), as the extension of conventional photothermal radiometry (PTR), is a popular and powerful non-destructive method for characterizing nonhomogeneous solids.[1–5] LITI and PTR have been successful in measuring quantitative geometric and thermophysical parameters of solid structures, such as case depths in hardened metals,[6,7] thermal conductivities and diffusivities[8–13] and their depth profiles,[8,14] and coating thicknesses.[9,15,16] A wide range of frequencies is used for characterizing such materials by means of frequency point scan measurements with a high resolution sampling rate integrated with hardware or software lock-in signal processing methods. There are some limitations to expanding these methods from point scan to area scan inspections with infra-red cameras currently available in the market. Unfortunately, the low frame rate of thermal infrared cameras is a disadvantage of conventional synchronous digital lock-in image processing, especially in the case of frequencies above the critical frequency determined by the maximum frame rate, f_{fr}, of the camera. Undersampling is required for frequencies $f > f_{fr}/4$, and very precise synchronization is needed for image sampling in this case. Failure to synchronize is a source of decreased signal-noise ratio (SNR) and image quality deterioration. A high SNR is especially important for quantitative measurements of photothermal parameters and structural features of materials. The development of thermal-wave radar imaging (TWRI) uses linear frequency modulation (LFM) chirps and has brought about significant improvement in dynamic range compared to conventional LITI.[17] This work introduces a special case of TWRI, single-frequency thermal-wave radar imaging (SF-TWRI). Frequency point scan application of SF-TWRI based on a swept sine software algorithm was reported earlier[7] and is now being extended into a thermographic technique for fast non-destructive imaging as described in this paper. SF-TWRI is a modality that allows the acquisition of pixel amplitude and phase signals over arbitrarily wide ranges of modulation frequencies at a high SNR. The image acquisition is free of sampling constraints and thus can obtain complete frequency scans for all camera pixels and perform quantitative data fits to thermal-wave theory[18] in order to extract quantitative non-destructive images of geometrical and/or thermophysical parameters of interrogated materials and structures. SF-TWRI output pixel signal distributions and whole images are compared with conventional LITI in applications involving quantitative thickness imaging of coatings deposited on two different substrates and the subsurface location of blind holes drilled in a steel block.

a)Electronic mail: mandelis@mie.utoronto.ca

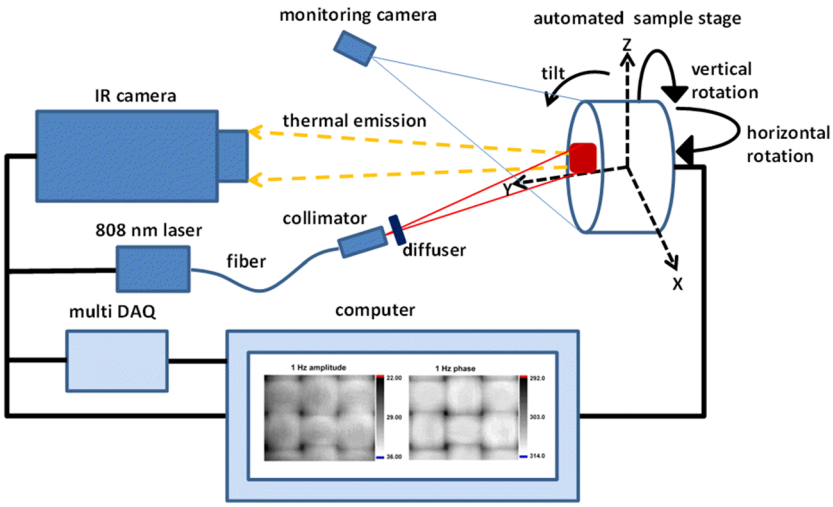

FIG. 1. Schematic diagram of the experimental LITI and SF-TWRI setup.

II. INSTRUMENTATION, EXPERIMENTAL, AND MATERIALS

A. Instrumentation

A schematic diagram of both LITI and TWRI setups which share the same instrumentation and other common features is shown in Fig. 1. The setup consists of a mid-infrared (MIR) camera (CEDIP Titanium model 520M), National Instruments data acquisition (DAQ) (model USB-6229), 45-W, 808-nm fiber-coupled laser (model JOLD-45-CPXF-1L), ThorLabs laser driver (model LDC 3065), and computer. For this investigation, the laser beam emerging from the fiber was collimated with a Thorlabs collimator F810SMA-780, homogenized and spread by a microlens array ED1-C20 from Thorlabs. The illuminated square area was ca. 3×3 cm^2 with inhomogeneity less than 5% over the entire imaged area. The desired waveforms for laser modulation, reference signals, and trigger signals were produced by the DAQ card under control of a LabView program which processes sampled images captured by means of conventional LITI or SF-TWRI image processing modality.

B. Lock-in and SF-TWR image processing

Signal process flow block diagrams of lock-in thermography (LIT) and thermal-wave radar (TWR) imaging are shown in Figs. 2(a) and 2(b), respectively. Camera sampling diagrams for the two techniques are shown in Figs. 3 and 4, respectively. The lock-in and TWR cross-correlation (CC) signal generation processes indicated in those figures are applied to each and every pixel of the camera. LITI digital processing for each pixel at harmonic modulation $\sin(2\pi ft)$ is performed according to the following equations:[1]

$$S^0(x,y) = \sum_{k=1}^{n} [I_k(x,y)\sin(2\pi f t_k)], \tag{1}$$

$$S^{90}(x,y) = \sum_{k=1}^{n} \{I_k(x,y)[-\cos(2\pi f t_k)]\}, \tag{2}$$

$$Amplitude\ LITI\ (x,y) = \frac{1}{n}\left\{[S^0(x,y)]^2 + [S^{90}(x,y)]^2\right\}^{0.5}, \tag{3}$$

$$Phase\ LITI\ (x,y) = \tan^{-1}\left(\frac{S^{90}(x,y)}{S^0(x,y)}\right). \tag{4}$$

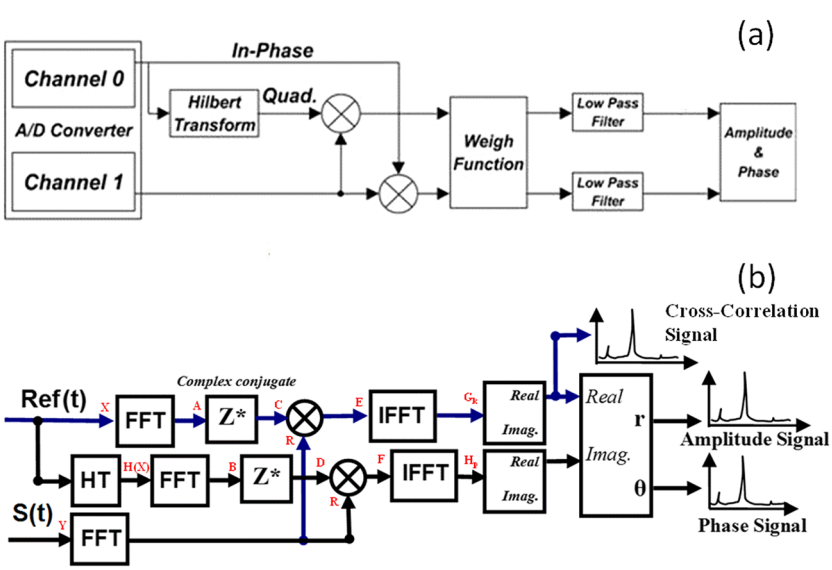

FIG. 2. Block diagram of LIT (a) and TWR (b) imaging modalities. HT stands for the Hilbert transform, FFT for fast Fourier transform, IFFT for inverse fast Fourier transform.

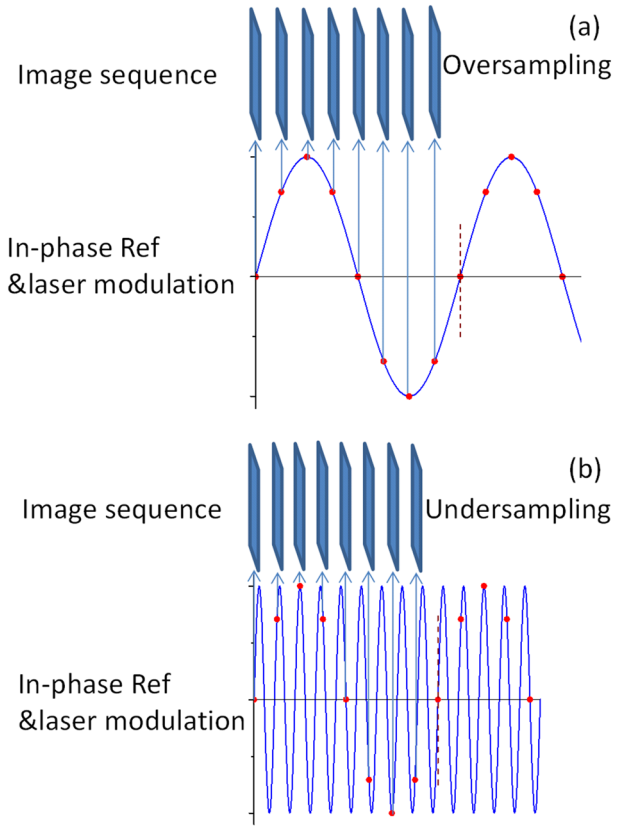

FIG. 3. LITI signal processing. The vertical dashed lines mark the beginning of the second lock-in period. (a) Conventional synchronous oversampling and (b) conventional synchronous undersampling.

Here, n is the number of frames per correlation cycle, $n \geq 4$, $I_k(x, y)$ is the thermal response of the (x, y) pixel, and $\sin(2\pi f t_k)$ is the reference signal. Synchronous correlation occurs at frequencies $f_{lock\text{-}in} = f_s(m + 1/n)$, where f_s is the sampling rate and m is an integer. Any multiples of the Nyquist frequency, $f_s/2$, should be avoided.[1] Oversampling takes place at $m = 0$, while undersampling of order m is triggered when $m \geq 1$, Fig. 3. In conventional camera frame correlation, n samples are distributed over one modulation period. For undersampling, one full sampling cycle is completed in more than one signal period with one frame obtained over one or more signal periods. In both oversampling and undersampling modes, the frame rate should be reduced below the maximum possible rate due to the unavailability of several desired frequencies or the long measurement times required for one full correlation cycle. These effects lead to low SNR which, however, improves with the reduction in frame rate.[1] Undersampling at high frequencies creates additional stringent requirements for synchronization. Timing accuracy requirements, especially at high undersampling orders, lead to additional reduction of the SNR. The result is that LITI is *not* an optimal option for shallow–depth imaging that requires high modulation frequencies. It should also be mentioned that changing the frame rate is necessary in order to adjust the position of sampling inside the signal period for going from oversampling to undersampling when scanning over wide frequency ranges. This is problematic with cameras without adjustable frame rate capability.

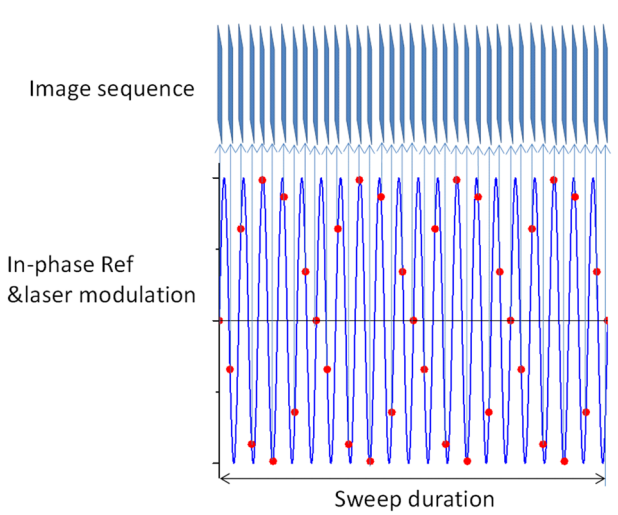

FIG. 4. SF-TWRI signal processing flowchart. A case of $f > f_{fr}/4$.

A possibility for eliminating the aforementioned stringent sampling synchronization requirements and substantially improving thermographic imaging at arbitrary frequencies (especially in the LITI undersampled high-frequency range) arises as a special case of TWR signal processing using a single-frequency sweep when the start and end frequencies coincide. The TWRI signal processing scheme for calculating CC is shown in Fig. 2(b). In that figure, the following alphanumeric definitions are made and used for numerical amplitude and phase computations:

$$A = FFT\,[X] = X_k = \sum_{n=0}^{N-1} x_n e^{-\frac{j2\pi kn}{N}}, \qquad k = 0, 1, \ldots, \mathrm{N}-1, \tag{5}$$

$$B = FFT\,\{[H[X]]\} = X_p = \sum_{r=0}^{N-1} x_r e^{-\frac{j2\pi pr}{N}}, \quad p = 0, 1, \ldots, \mathrm{N}-1, \tag{6}$$

$$R = FFT[Y] = Y_l = \sum_{m=0}^{N-1} y_m e^{-\frac{j2\pi lm}{N}}, \qquad l = 0, 1, \ldots, \mathrm{N}-1, \tag{7}$$

$$C = A^* = \sum_{n=0}^{N-1} x_n e^{\frac{j2\pi kn}{N}}, \quad k = 0, 1, \ldots, \mathrm{N}-1, \tag{8}$$

$$D = B^* = \sum_{r=0}^{N-1} x_r e^{\frac{j2\pi pr}{N}}, \quad p = 0, 1, \ldots, \mathrm{N}-1, \tag{9}$$

$$E = (R) \times (C) = Y_l X_k^* = \sum_{n=0}^{N-1} x_n \sum_{m=0}^{N-1} y_m e^{-\frac{j2\pi(lm-kn)}{N}}, \tag{10}$$

$$F = (R) \times (D) = Y_l X_p^* = \sum_{r=0}^{N-1} x_r \sum_{m=0}^{N-1} y e^{-\frac{j2\pi(lm-pr)}{N}}, \tag{11}$$

$$G_k = \frac{1}{N} \sum_{n=0}^{N-1} E_n e^{-\frac{j2\pi kn}{N}}, \quad k = 0, 1, \ldots, \mathrm{N}-1, \tag{12}$$

$$H_p = \frac{1}{N} \sum_{n=0}^{N-1} F_n e^{-\frac{j2\pi pn}{N}}, \quad p = 0, 1, \ldots, \mathrm{N}-1, \tag{13}$$

$$Amplitude\ TWRI(x, y) = \max(real(G)), \tag{14}$$

$$Phase\ TWRI(x, y) = \tan^{-1}\left(\frac{real(H_0)}{real(G_0)}\right). \tag{15}$$

Starred quantities indicate complex conjugation. In practice, TWR signals are processed as follows: a reference chirp signal

in the frequency range f_1-f_2 and of duration T is generated to modulate the laser. The reference signal and the photothermal response chirp signal from the camera are acquired through the data acquisition card and Ethernet card. Then the fast Fourier transform (FFT) of the TWR response signal (Y) in chirp form and the FFT complex conjugate of the reference signal [X, H(X)] are computed, and both signals are multiplied (E, F) to calculate the inverse FFT of the effective response signal (G, H). As a last step, the amplitude and phase of each pixel are calculated and displayed. *Using the same frequency for the start and end of a TWRI sweep allows the calculation of the amplitude and phase at that frequency and the measurement of detailed pixel frequency dependencies by scanning over a wide range of frequencies at arbitrary intervals similar to photothermal radiometry, free from critical frequency exclusion, inter-frequency interval constraints, and upper limits imposed by sampling*. The synchronization method used in SF-TWR works in any frequency range, excluding multiples of the Nyquist frequency (half the sampling frequency). Furthermore, the camera frame rate can be set to maximum for all types of cameras used in SF-TWRI, as opposed to the exclusion of some low-grade cameras from conventional sampling-limited LITI. This feature guarantees the highest possible SNR because it generates the maximum number of frames for amplitude and phase calculations determined by the sweep duration, T, (the measurement time) independent of the selected modulation frequency. It should be mentioned that the correlation cycle needs to start after establishing a steady-state modulated temperature profile for both methods to avoid distortion of the harmonic thermal wave. This time duration may be at least 1 s, enough for most solids to attain modulated thermal steady state. No conventional undersampling is needed, and maximum frequency is limited only by the camera frame integration time. Signal processing is done through CC, not through the lock-in process.[19] As a result, SF-TWR provides a uniform, continuous approach below and above the critical frequency $f_{fr}/4$. Critical parameters such as single-frequency sweep duration and camera frame rate are operator controlled and not dictated by sampling requirements. The preferable frame rate is the maximum rate of the camera used. The net outcome is higher SNR for SF-TWRI than for conventional LITI, with the additional advantage that the measurement time of TWRI is less than LITI especially within the undersampling range of LITI.

1. Materials

Three kinds of samples were used in the first applications of SF-TWRI: a steel block with blind holes drilled at various subsurface depths, an aluminum substrate, and a polymer (polyetherketone; PEEK) substrate, both with Co-P alloy coatings. Quantitative images of coating thicknesses and distances of blind holes from the surface of the steel block were generated from combined SF-TWRI frequency scans and a theoretical multi-layer model with grouped parameters.[20]

III. RESULTS AND DISCUSSION

For comparison of the two imaging methods, a 0.4-mm deep subsurface blind hole was investigated at 1 Hz, 10 Hz, and 16 Hz. SF-TWRI amplitudes and phases are shown in Fig. 5. Sweep duration was 1 s at 1 Hz and 10 Hz, and 2 s at 16 Hz. The frame rate was 360 fr/s at all frequencies. Due to

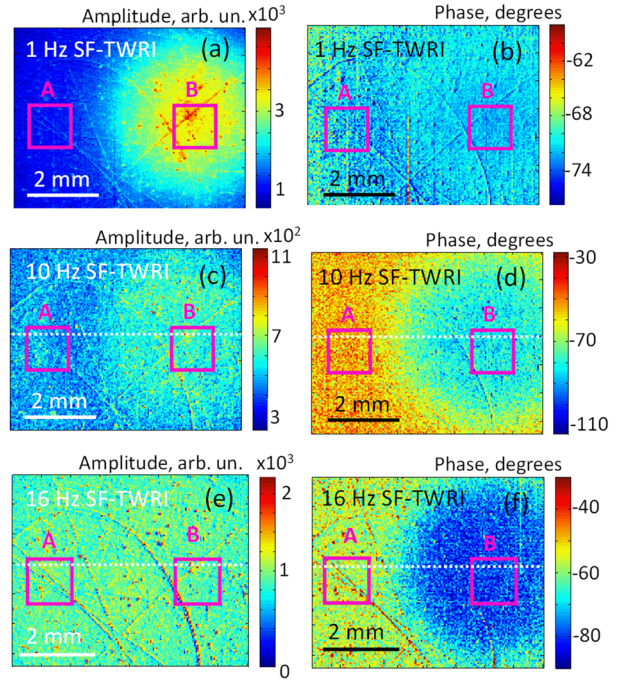

FIG. 5. Amplitude and phase SF-TWRI images of a steel block with a 0.4-mm deep subsurface blind hole at 1 Hz (sweep duration: 1 s) [(a) and (b)]; 10 Hz (sweep duration: 1 s) [(c) and (d)]; and 16 Hz (sweep duration: 2 s) [(e) and (f)] and frame rate 360 fr/s for all frequencies. Regions A and B represent areas without a hole and with a subsurface hole, respectively.

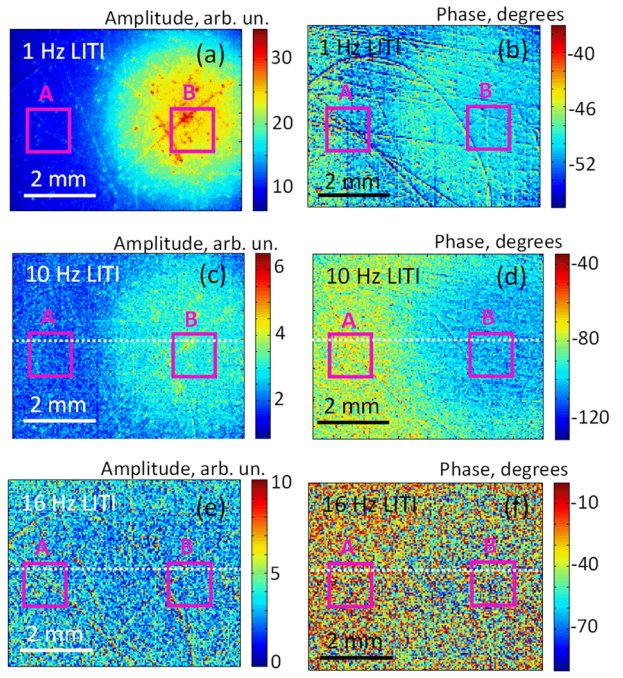

FIG. 6. Amplitude and phase LITI images of the same sample as shown in Fig. 5. [(a) and (b)] 1 Hz, 1 image averaged with frame rate 360 fr/s; [(c) and (d)] 10 Hz, 10 images averaged with frame rate 360 fr/s; [(e) and (f)] 16 Hz, 1 image averaged over two correlation cycles, undersampled with frame rate 15 fr/s.

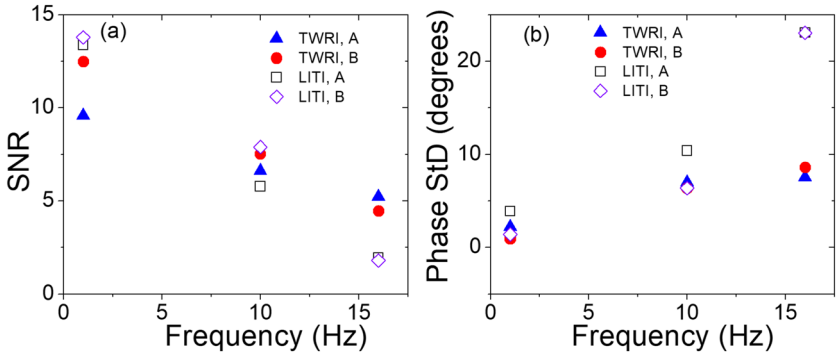

FIG. 7. Amplitude SNR (a) and phase StD (b) of SF-TWRI and LITI pixel distribution dependencies on frequency for areas A and B.

the decreased thermal diffusion length at increased frequencies, amplitude contrast of the hole practically disappeared at 16 Hz, as expected. The phase image was the most sensitive channel and clearly shows the hole at 16 Hz. For a more detailed analysis, two areas A and B were chosen in Fig. 5 corresponding to a part of the steel block without a blind hole (semi-infinite substrate) and inside an area with a subsurface blind hole, respectively.

In the LITI case, Fig. 6, the contrast was similar for 1 Hz and 10 Hz modulation, but it disappeared at 16 Hz from both the amplitude and phase. The numbers of averaged LITI images were 1 at 1 Hz, 10 at 10 Hz, and 1 over 2 correlation cycles at 16 Hz, chosen so as to keep the sum of the measurement time of the correlation cycles the same as for the corresponding SF-TWRI sweep duration for correct comparison of the two methods. 1 Hz and 10 Hz LIT images were the results of oversampling with frame rate 360 fr/s, the same as for SF-TWR images. In both cases, the same number of frames was used for data processing, and this explains the similarities of amplitude and phase contrast between the two modalities. However, at 16 Hz, LITI was the result of undersampling with 15 fr/s frame rate and 30 frames during 2 s measurement of two iteration cycles, as opposed to 360 fr/s and 720 frames during 2 s for the corresponding SF-TWRI. As can be clearly seen in Figs. 5 and 6, SF-TWRI has major advantages for detecting subsurface inhomogeneities in solids in the frequency range above the LIT critical (undersampling) threshold.

The scatter in amplitude and phase in regions A and B from Figs. 5 and 6 with and without blind holes, respectively, is much less for SF-TWRI than LITI at 16 Hz, while it is similar for both methods (somewhat less for SF-TWRI) in the case of the same number of frames at low frequencies as also shown in the amplitude SNR and phase standard deviation (StD) frequency dependencies of Fig. 7. LITI at 16 Hz was performed with undersampling that led to increased measurement time by increasing the number of averages to achieve the same quality SNR as SF-TWRI. The estimated amplitude SNR for the two areas A and B is much lower for LITI in the undersampled range than that for SF-TWRI at the same frequency; furthermore, the StD of the LITI phase is much larger mainly due to the larger number of data points involved in the SF-TWRI algorithm. These observations are also confirmed by comparison of single-line pixel profiles across the images in Figs. 8 and 9. These profiles very clearly show marginally higher SF-TWRI

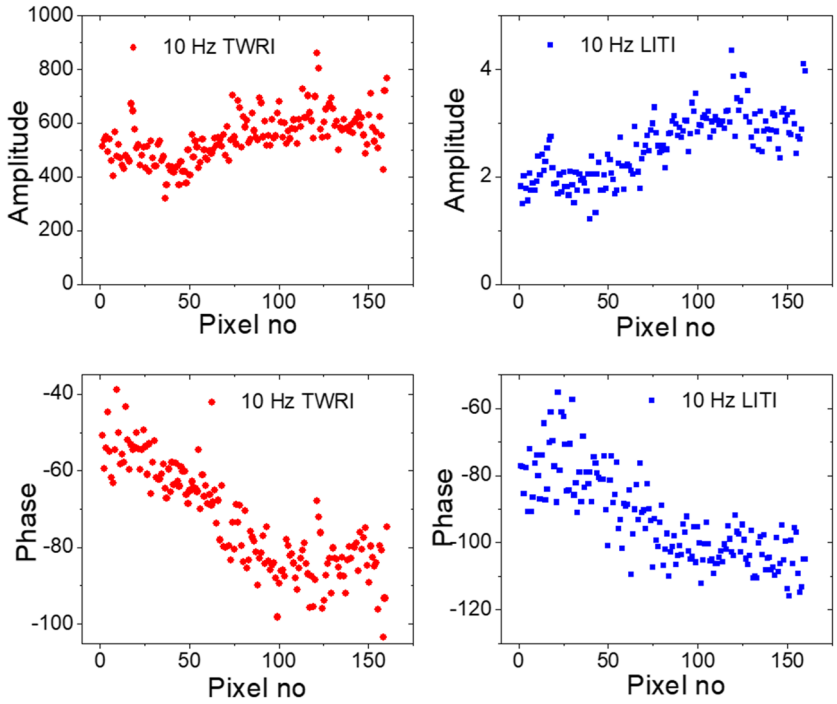

FIG. 8. Profile comparison between SF-TWRI and LITI amplitude and phase distributions at 10 Hz for the horizontal dotted pixel line shown in Figs. 5(c), 5(d), 6(c), and 6(d).

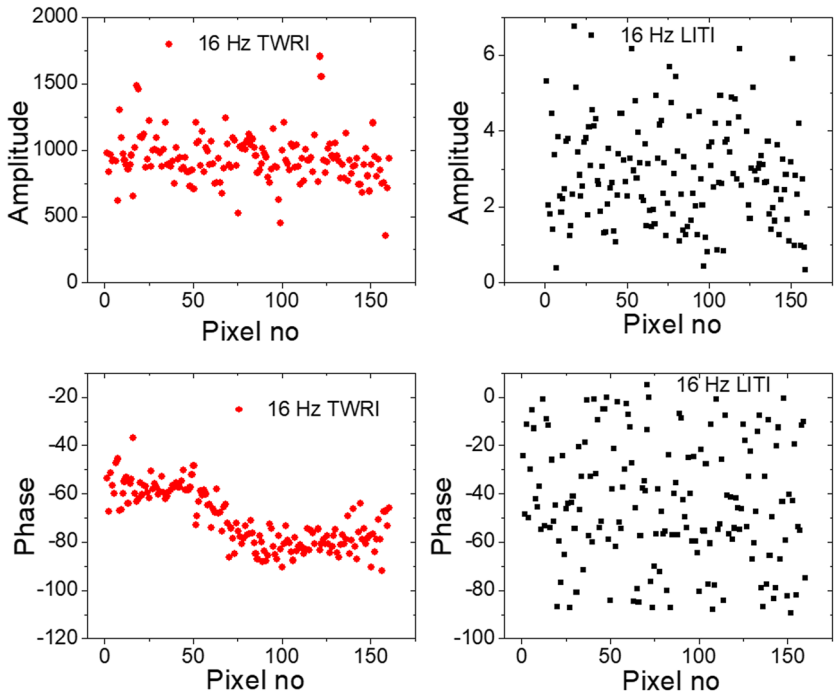

FIG. 9. Profile comparison between SF-TWRI and LITI amplitude and phase distributions at 16 Hz for the horizontal dotted pixel line shown in Figs. 5(e), 5(f), 6(e), and 6(f).

SNR for the 10 Hz image and substantially higher SNR for the 16-Hz image than LITI. The reason is the insufficient number of synchronized data points in processing conventional LIT images, a trend that worsens with increasing frequency.

In conclusion, the better quality of SF-TWRI is due to the larger number of frames involved in the CC process than in the lock-in process involved in LITI, as well as the absence of undersampling requirements for data processing in the former technique. SF-TWRI does not require frame rate changes over wide frequency scans and/or across the critical frequency and allows using the maximum frame rate regardless of modulation frequency. These attributes render this method very attractive for quantitative thermographic imaging and evaluation of various material parameters through images reconstructed from series of frequency scans.

IV. THEORETICAL ANALYSIS OF A MULTILAYER SYSTEM

For a demonstration of quantitative SF-TWR imaging of coatings, a one-dimensional two-layer model was used.[18,20] A schematic representation of the photothermal model is shown in Fig. 10. The modulated thermal-wave field on the surface

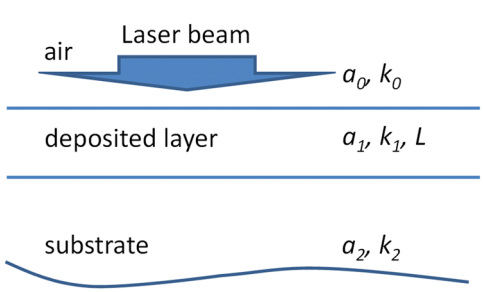

FIG. 10. Schematic cross-sectional geometry of a one-dimensional two-layer system photothermal model.

with grouped parameters can be expressed as[18,20]

$$\Delta T_1(0,f) = \frac{P_2(1-\gamma_{01})}{P_1(1-\gamma_{02})}\frac{(1-\gamma_{21}e^{-2(i+1)\sqrt{\pi f}Q_1})}{(1+\gamma_{21}e^{-2(i+1)\sqrt{\pi f}Q_1})}, \tag{16}$$

where $Q_1 = \frac{L}{\sqrt{\alpha_1}}$, $P_m = \frac{k_m}{\sqrt{\alpha_m}}$, $b_{mn} = \frac{P_m}{P_n}$, $\gamma_{mn} = \frac{b_{mn}-1}{b_{mn}+1}$. m, $n = 0$, 1, 2 refers to air, coating layer, and substrate, respectively. k_m is the thermal conductivity of the corresponding layer, α_m is its thermal diffusivity, and L is the thickness of the coating layer.

Normalization by a semi-infinite opaque substrate is necessary to take into account the instrumental transfer function. The Q_1 factor in Eq. (16) is the only sensitive parameter to layer thickness and can be most reliably measured through frequency-response best-fitting to the theory. Using the lumped parameter Q_1 leads to a reduction in the number of parameters by multi-parameter fitting and strengthens the uniqueness of the fit[20] which, in turn, allows a significant reduction in the standard deviation of the calculated values in the presence of noise.

SF-TWRI was used to reconstruct quantitative images of the coating Co-P alloy layer thicknesses on aluminum and polyetherketone (PEEK) substrates. The phase images of the coated Al substrate at three frequencies are shown in Fig. 11. The phase was chosen as the preferred signal channel over the amplitude due to its higher sensitivity to deeper inhomogeneities and its weak or no dependence on the optical quality of the surface. Purely thermally inhomogeneous distributions are observed as phase contrast at all three frequencies. Although phase lag involves information about coating layer thickness distributions, quantitative images can only be derived from full frequency scans and theoretical best fits.[17,19] Two small areas with different coating thicknesses, C and D, were chosen to demonstrate differences in frequency dependence. The thickness of area D coating was

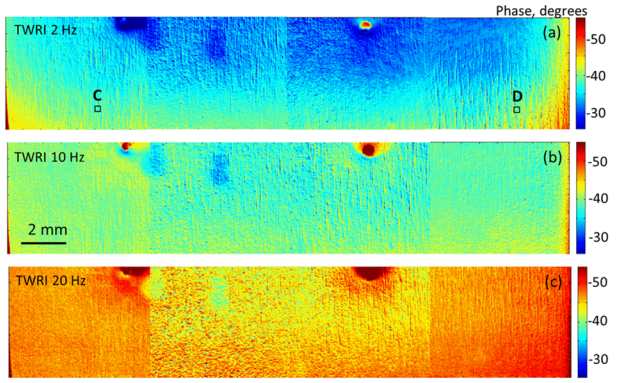

FIG. 11. (a) 2-Hz, (b) 10-Hz, and (c) 20-Hz SF-TWR phase images of a sample of a deposited Co-P alloy layer on an aluminum substrate.

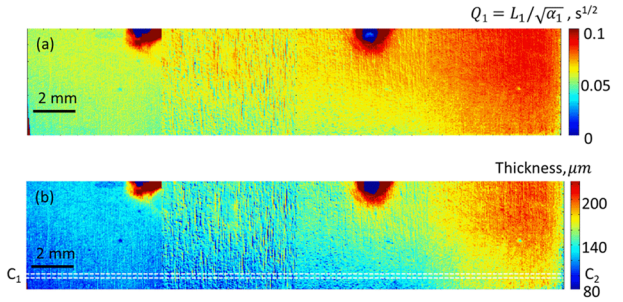

FIG. 13. Images of Q_1-parameter (a) and estimated thickness (b) of the coating layer deposited on the aluminum substrate.

larger than that of area C. Data best-fitting was carried out according to the two-layer model with grouped parameters, Eq. (16). An example of fitting phase responses averaged over the 6 × 6 pixel regions C and D in the investigated sample is presented in Fig. 12. To take into account the instrumental transfer function,[9] the data were normalized to a thick ("semi-infinite") Zr substrate. The Zr substrate was measured at the same conditions as the investigated sample. Phase normalization was performed by subtracting the phase of Zr from the phase of the sample for each image pixel. The key feature in the phase frequency dependence is the minimum, the frequency position of which depends on the thickness of the layer, assuming constant thermal diffusivity across the coating.[9] The minimum shifts to lower frequencies for thicker layers.

The Q_1-parameter image, reconstructed as the result of best-fitting each pixel frequency response to the thermal-wave theory, Eq. (16), using 16 frequency images, is shown in Fig. 13(a). To convert the Q_1-parameter image into the coating layer thickness, a point with a known thickness was chosen and the thermal diffusivity α was calculated using the best-fitted Q_1 value. The thus calculated diffusivity $\alpha = 5.305 \times 10^{-6}$ m^2/s was used for the entire coated layer and for the calculation of the layer thickness distribution, shown in Fig. 13(b). For similar applications, the diffusivity of deposited layers can be found either from the literature or from independent measurements (preferred) on the particular coating as in the present case. For validation of the reconstructed coating thickness image, a comparison between the directly measured thickness profile along the straight-line strip C_1C_2 in Fig. 13(b) and that calculated from the foregoing procedure shows very good consistency, Fig. 14. The apparent small divergence in regions close to the edges on both sides of the strip is likely due to a breakdown in the assumption of constant thermal diffusivity and/or one-dimensionality in those regions. Because the presence of the edges was not taken into account in the camera measurements, the thermal wave confinement would decrease the effective diffusivity within a thermal diffusion length from the edge, and the 1-D theory with constant diffusivity predicted a smaller thickness as shown in Fig. 14. It is well known that the presence of edges increases photothermal signals.[18,21]

The other type of coating-substrate polymer PEEK sample was imaged as the reconstruction from 23 normalized frequency image dependencies to the final thickness image (Fig. 15). The diffusivity, $\alpha = 2.54 \times 10^{-5}$ m^2/s, that was calculated as described above was used for the entire coated layer. An example of single pixel frequency fitting during the reconstruction process akin to Fig. 12 is shown in Fig. 16. Both results, Figs. 13 and 15, demonstrate the effectiveness of

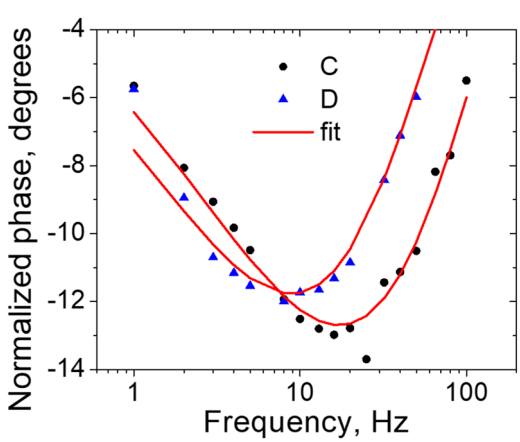

FIG. 12. Normalized mean phase dependencies on frequency and best fits at two 6 × 6 pixel locations C and D in Fig. 11. The fitted parameter Q1 is 5.18×10^{-2} s$^{0.5}$ and is 7.27×10^{-2} s$^{0.5}$ for locations C and D correspondingly.

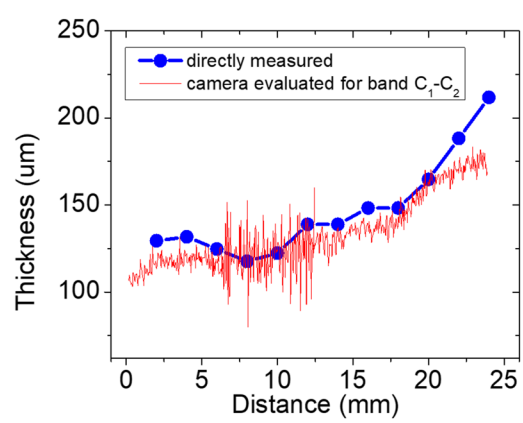

FIG. 14. Directly measured and camera-image-evaluated deposited layer thickness profiles.

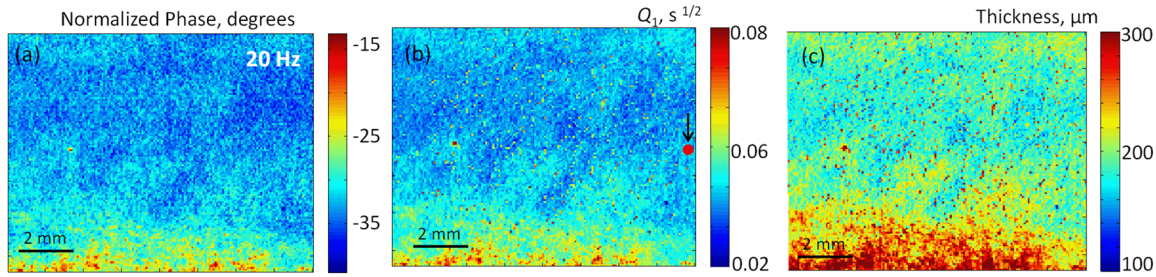

FIG. 15. Normalized images at (a) 20 Hz; (b) fitted Q_1-parameter; and (c) estimated thickness of a Co-P layer deposited on polymer PEEK.

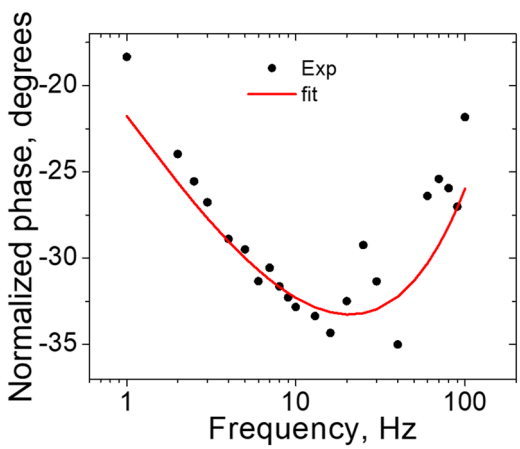

FIG. 16. Normalized phase dependence on frequency and best fit to Eq. (16) of the pixel at the arrow location (red point) shown in Fig. 15(b). The fitted parameter Q_1 is 3.8×10^{-2} $s^{0.5}$.

SF-TWRI in producing quantitative thickness images of coatings on different types of substrates.

Finally, images of the Q_1-parameter and several blind-hole depth distributions in steel are presented in Fig. 17. The thicknesses of the overlayers above the holes were calculated from the fitted Q_1-parameter, using the diffusivity value, $\alpha = 15.6 \times 10^{-6}$ m^2/s, estimated from the known thickness (0.4 mm) of the overlayer above one of the holes. This value is very close to the literature value of thermal diffusivity of AISI 1010 steel, $\alpha = 18.8 \times 10^{-6}$ m^2/s.[22] The calculated thicknesses were 0.6 mm for the 0.6 mm hole and 1.14 mm for 1 mm hole. The small thickness overestimation of the 1-mm hole is due to the deviation from the one-dimensionality. Sideways diffusion not accounted for in the 1-D theory gives an effective higher diffusivity, so for a given phase lag, one measures a larger effective thickness as seen in the strip along the edge of the hole in Fig. 17. To avoid discrepancies due to dimensionality and edge geometries, a calibrated measurement gives very good approximation in quantitative SF-TWR images of the subsurface hole depths.

V. CONCLUSIONS

Single-frequency thermal-wave radar (SF-TWR) was introduced as a significant improvement over conventional lock-in thermography (LIT) for quantitative non-destructive imaging, especially at high modulation frequencies. It can be implemented with the same setup as LITI with only software signal generation and processing changes. The SNR is higher for SF-TWRI than for LITI at high frequencies above the critical undersampling value because SF-TWRI operates on cross-correlation signal processing and not on waveform sampling (lock-in imaging) principles. It was shown that SF-TWRI is a *fast quantitative* non-destructive imaging (NDI) technique. A first application was demonstrated in non-destructive imaging of deposited coating-on-engineering-material-substrate thickness images and in depth imaging of subsurface blind holes in steel. Using camera frequency scans over extended ranges not limited by the lock-in process allows reconstructing quantitative thermophysical and geometric parameter images of materials. The SF-TWR

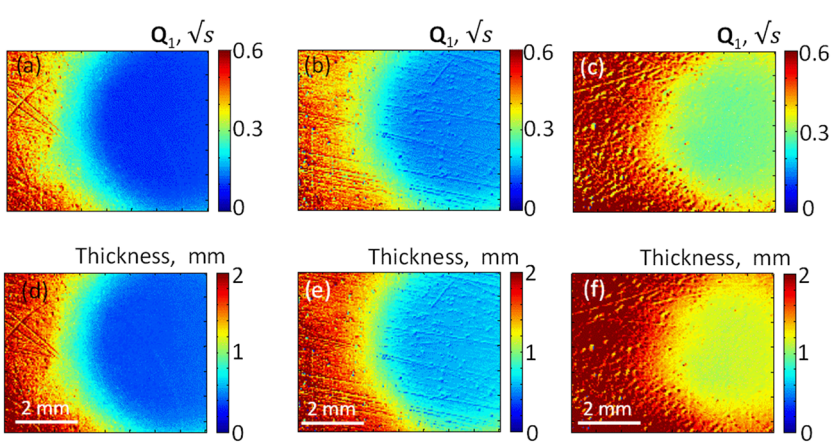

FIG. 17. Images of Q_1-parameter (a)–(c) and estimated blind hole depths in steel (d)–(f). [(a) and (d)] 0.4 mm, [(b) and (e)] 0.6 mm, [(c) and (d)] 1 mm.

technique gives rise to the possibility of enabling thermal cameras with fixed frame rates to perform dynamic imaging, competing with top-of-the-line infrared cameras. It thus represents a next-generation thermography method with superior features for imaging important classes of thin layers, materials, and components that require high-frequency thermal-wave probing well above today's available infrared camera technology frame rates.

ACKNOWLEDGMENTS

A. Mandelis gratefully acknowledges the NSERC Strategic Grants Program, an NSERC Discovery grant, and the Canada Research Chairs Program for financial support.

[1] O. Breitenstein, W. Warta, and M. Langenkamp, *Lock-in Thermography*, 2nd ed. (Springer, 2010).
[2] D. Wu and G. Busse, "Lock-in thermography for nondestructive evaluation of materials," Rev. Gen. Therm. **37**, 693–703 (1998).
[3] C. Wallbrink, S. A. Wade, and R. Jones, "The effect of size on the quantitative estimation of defect depth in steel structures using lock-in thermography," J. Appl. Phys. **101**, 104907 (2007).
[4] C. Meola, G. M. Carlomagno, A. Squillace, and G. Giorleo, "Non-destructive control of industrial materials by means of lock-in thermography," Meas. Sci. Technol. **13**, 1583–1590 (2002).
[5] C. Meola, G. M. Carlomagno, A. Squillace, and A. Vitiello, "Non-destructive evaluation of aerospace materials with lock-in thermography," Eng. Failure Anal. **13**, 380–388 (2006).
[6] C. H. Wang and A. Mandelis, "Case depth determination in heat treated steel products using photothermal radiometric interferometric phase minima," NDT&E Int. **40**, 158–167 (2007).
[7] X. Guo, K. Sivagurunathan, J. Garcia, A. Mandelis, S. Giunta, and S. Milletari, "Laser photothermal radiometric instrumentation for fast in-line measurements of industrial steel hardness inspection and quality control," Appl. Opt. **48**(7), C11–C23 (2009).
[8] A. Mandelis, "Diffusion-wave laser radiometric diagnostic quality control technologies for materials NDE/NDT," NDT&E Int. **34**, 277–287 (2001).
[9] J. A. Garcia, A. Mandelis, B. Farahbakhsh, C. Lebowitz, and I. Harris, "Thermophysical properties of thermal sprayed coatings on carbon steel substrates by photothermal radiometry," Int. J. Thermophys. **20**(5), 1587–1602 (1999).
[10] A. Cifuentes, A. Mendioroz, and A. Salazar, "Simultaneous measurements of the thermal diffusivity and conductivity of thermal insulators using lock-in infrared thermography," Int. J. Therm. Sci. **121**, 305–312 (2017).
[11] C. Boué and S. Holé, "Infrared thermography protocol for simple measurements of thermal diffusivityand conductivity," Infrared Phys. Technol. **55**, 376–379 (2012).
[12] K. Strzałkowski, M. Streza, and M. Pawlak, "Lock-in thermography versus PPE calorimetry for accurate measurements of thermophysical properties of solid samples: A comparative study," Measurement **64**, 64–70 (2015).
[13] P. W. Nolte, T. Malvisalo, A. C. Rimbach, F. Steudel, B. Ahrens, and S. Schweizera, "Lock-in thermography for the development of new materials," Mater. Today: Proc. **4**, S128–S134 (2017).
[14] R. Cellorio, E. Apiñaniz, A. Mendioroz, A. Salazar, and A. Mandelis, "Accurate reconstruction of the thermal conductivity depth profile in case hardened steel," J. Appl. Phys. **107**, 083519 (2010).
[15] R. Shrestha and W. Kim, "Evaluation of coating thickness by thermal wave imaging: A comparative study of pulsed and lock-in infrared thermography—Part I: Simulation," Infrared Phys. Technol. **83**, 124–131 (2017).
[16] J.-Y. Zhang, X.-B. Meng, and Y.-C. Ma, "A new measurement method of coatings thickness based on lock-in thermography," Infrared Phys. Technol. **76**, 655–660 (2016).
[17] N. Tabatabaei and A. Mandelis, "Thermal-wave radar: A novel subsurface imaging modality with extended depth-resolution dynamic range," Rev. Sci. Instrum. **80**, 034902 (2009).
[18] A. Mandelis, *Diffusion-Wave Fields: Mathematical Methods and Green Funktion* (Springer, 2001).
[19] G. Busse, D. Wu, and W. Karpen, "Thermal wave imaging with phase sensitive modulated thermography," J. Appl. Phys. **71**, 3962 (1992).
[20] X. Guo, A. Mandelis, J. Tolev, and K. Tang, "Photothermal radiometry parametric identifiability theory for reliable and unique nondestructive coating thickness and thermophysical measurements," J. Appl. Phys. **121**, 095101 (2017).
[21] L. C. Aamodt and J. C. Murphy, "Effect of 3-D heat flow near edges in photothermal measurements," Appl. Opt. **21**, 111–115 (1982).
[22] See https://www.newagepublishers.com/samplechapter/000915.pdf for AISI 1010 Carbon Steel thermal diffusivity.